Synthesis of Nanoparticles-Deposited Double-Walled TiO$_2$-B Nanotubes with Enhanced Performance for Lithium-Ion Batteries

Jie Qu,[†,‡] Jacqueline E. Cloud,[‡] Yongan Yang,*,[‡] Jianning Ding,*,[†] and Ningyi Yuan[†]

[†]Center for Low-Dimensional Materials, Micro-Nano Devices and System, Changzhou University, Jiangsu Key Laboratory for Solar Cell Materials and Technology, No. 1 Gehu Road, Changzhou, 213164, China

[‡]Department of Chemistry and Geochemistry, Colorado School of Mines, 1012 14th Street, Golden, Colorado 80401, United States

S *Supporting Information*

ABSTRACT: A one-step hydrothermal method, followed by calcination at 300 °C in an argon atmosphere, has been developed to synthesize TiO$_2$-B nanoparticles/double-walled nanotubes (NP/DWNT) and TiO$_2$-B nanoparticles/multiple-walled nanotubes (NP/MWNT). To the best of our knowledge, this is the first synthesis of TiO$_2$-B NP/NT hierarchical structures. Both NP/DWNT and NP/MWNT show high performance as anode materials for lithium-ion batteries, superior to their counterparts of DWNT and MWNT, respectively. Among all the four materials studied herein, NP/DWNT demonstrates the highest discharge−charge capacity, rate capability, and cycling stability. The enhancement due to the NP loading results from the increased surface areas, the improved kinetics, and the decreased transport distance for both electrons and Li ions. The charge capacity at high rates lies in the intercalation pseudocapacitance originating from fast Li-ion transport through the infinite channels in TiO$_2$-B. The superiority of DWNT materials versus MWNT materials is ascribed to the thinner walls, which provide a shorter distance for Li-ion transport through the radial direction.

KEYWORDS: *lithium-ion batteries, TiO$_2$-B, double-walled nanotubes, nanoparticles, high-rate performance, hydrothermal synthesis*
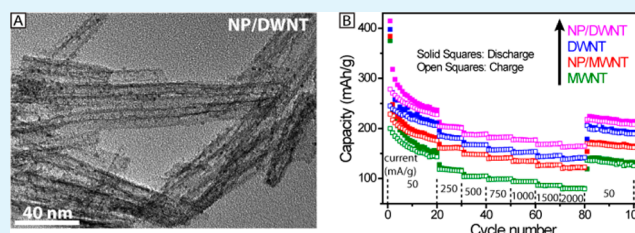
1. INTRODUCTION

Lithium-ion batteries (LIBs), currently the most advanced rechargeable batteries, are ubiquitous in portable electronic devices. The interest in developing new generations of LIBs to power large-scale devices, such as electric vehicles and hybrid electric vehicles, has been increasing in the past two decades.[1,2] Such applications require electrode materials with high energy density, long cycle life, and high rate capability.[3−5] Titanium dioxide (TiO$_2$) as an anode material has attracted significant attention due to its cost-effectiveness, nontoxicity, high rate capability, dependable safety, and high chemical stability.[6−11] Among all polymorphs, TiO$_2$-B is the most promising and has been intensively studied by many researchers,[7,12−14] since the first synthesis by Marchand et al. in 1980 by calcining the K$^+$/ H$^+$ ion exchanged K$_2$Ti$_4$O$_9$.[15,16] TiO$_2$-B is composed of corrugated sheets of edge- and corner-sharing TiO$_2$ octahedra that are linked together by bridging oxygen atoms to form a three-dimensional network.[16−20] This structure possesses more open voids and parallel channels than in rutile, anatase, or brookite, rendering TiO$_2$-B an excellent host material for Li-intercalation.[18,21] Three types of sites for Li-ion intercalation have been identified in the literature, denoted as A1 sites, A2 sites, and C sites, respectively.[20] In one unit cell, the four A1 sites are the space coordinated in 5-fold symmetry with oxygen atoms and sit in the two (003) planes; the four A2 sites are the space also coordinated in 5-fold symmetry with oxygen atoms but sit in the two (001) planes; and the two C sites are the

space coordinated in planar 4-fold symmetry with oxygen atoms.[20] The full occupation of all 10 sites by Li ions renders a composition of Li$_{1.25}$TiO$_2$.[20,22,23] As a result, TiO$_2$-B presents faster charge/discharge rates, higher charge capacity, and superior cyclability compared with the other three polymorphs,[16,19,24,25] without significant distortion of the structure.[15,16]

Besides the aforementioned crystal structure, other factors (including sizes, shapes, crystallinity, and architectural arrangement) are also important for the electrode performance.[26,27] TiO$_2$ nanoparticles (NPs), which are easy to synthesize, enable fast reaction kinetics of Li-ion storage due to their high specific surface areas and abundant grain boundaries.[9,28−32] When the particle sizes are decreased below 10 nm in diameter, the achievable charge capacity can be significantly enhanced, extending the threshold (335 mAh/g) of the Li$_x$TiO$_2$ solid solution.[33,34] The extra charge capacity in this dimensional regime originates from the significant contribution from the pseudocapacitance due to the Faradaic reactions on particle surfaces. Moreover, the pseudocapacitive process at the liquid/ solid interface is much faster than the Li-ion intercalation process inside the bulk solid; thus, TiO$_2$-B NPs are very desirable for high charge/discharge rates.[30]

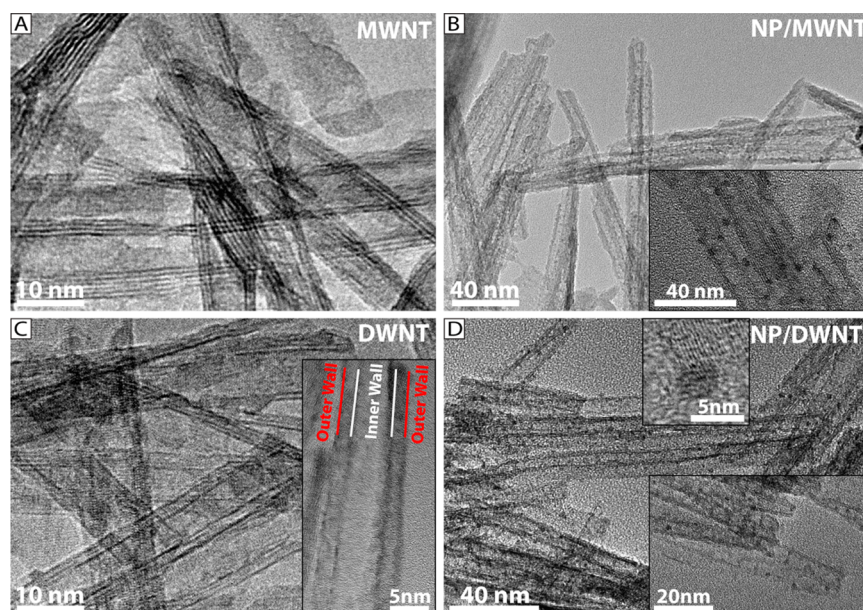**Figure 1.** TEM images of four types of TiO$_2$-B based materials, for which, during the hydrothermal process, the experimental conditions are 140 °C and 40 mL of NaOH solution for MWNT (A), 140 °C and 80 mL of NaOH solution for NP/MWNT (B), 150 °C and 40 mL of NaOH solution for DWNT (C), and 150 °C and 80 mL of NaOH solution for NP/DWNT (D).

On the other hand, one-dimensional (1D) nanostructures, including nanowires, nanorods, nanotubes, and their arrays, enable faster electron transport and Li-ion insertion/extraction as well as improved ability than NPs to accommodate the volume expansion, due to their specific geometric characteristics.[14,35−37] However, such nanostructures have smaller surface areas and fewer porous microstructures compared with NPs, especially when they have large radial dimensions and small aspect ratios or form dense arrays.[38] Hierarchical structures made by loading NPs onto 1D nanostructures, particularly nanotubes (NTs), can take advantages of both moieties and have been demonstrated to be an effective way to enhance materials' electrochemical performance in many systems.[39−45]

TiO$_2$-B NTs were first synthesized by Armstrong et al. in 2005 using a hydrothermal technique.[46] The first step is to load anatase (a-TiO$_2$) powder and concentrated NaOH solution in an autoclave vessel and keep the vessel at 150 °C for 72 h. The second step is to wash the solid product with an HCl solution and further calcine at 400 °C for 5 h. In the past decade, many research groups have modified this protocol in order to explore various applications of TiO$_2$-B NTs and understand the formation mechanism.[47−51] Studies show that TiO$_2$-B NTs are likely to be produced via a series of morphological transition from 3D particles, through 2D nanosheets, and then to 1D NTs via sheet scrolling.[48−51] The critical conditions are the hydrothermal temperature, the amount and concentration of NaOH, reaction time, and calcination temperature.[47,51−53] In most cases, the obtained TiO$_2$-B NTs are multiwalled; recently, some of the authors of this article (Qu, Ding, and Yuan) succeeded in synthesizing double-walled NTs by mainly controlling the amount and concentration of NaOH.[12] Nevertheless, the synthesis of TiO$_2$-B NP/NT hierarchical structures has not been reported.

Herein, we present a simple one-step hydrothermal method for synthesizing two novel materials of TiO$_2$-B nanoparticles-deposited/double-walled nanotubes (NP/DWNT) and nano-particles-deposited/multiwalled nanotubes (NP/MWNT) hier-archical structures, where the TiO$_2$-B NPs are about 3 nm in diameter and the TiO$_2$-B NTs are ∼10 nm × 100−200 nm (diameter × length). These NP/NT hierarchical structures exhibit significantly enhanced electrode performance, including charge capacity, rate capability, and cyclability, compared with their counterparts of DWNTs and MWNTs. The enhancement mechanism is discussed.

2. EXPERIMENTAL SECTION

2.1. Chemicals. Sodium hydroxide (NaOH, pellets, anhydrous, 98%) and hydrochloric acid (HCl, 36%) were purchased from Aladdin. Anatase TiO$_2$ (a-TiO$_2$, 25 nm, 99.8%), lithium ribbon (Li, 99%), acetylene black (C, 35−45 nm in grain sizes), polyvinylidene fluoride (PVDF, >99.5%), and N,N-dimethylformamide (DMF, anhydrous, 99.8%) were purchased from Sigma-Aldrich. The electrolyte of 1 M lithium hexafluorophosphate (LiPF$_6$) in ethyl carbonate/diethyl carbonate (EC/DEC, weight ratio of 1:1) was purchased from BASF. All chemicals were used as received.

2.2. Materials Synthesis and Characterization. TiO$_2$-B multi-walled nanotubes (MWNT): First, a-TiO$_2$ powder (3 g) was added to an aqueous solution of NaOH (10 M, 40 mL) in a beaker. After sonicating the beaker in an ultrasonic bath for 0.5 h, the resulting suspension was transferred to a Teflon-lined autoclave and heated at 140 °C for 48 h. The product was collected and rinsed with distilled water, 0.1 M HCl, and then distilled water again until the pH value of the elute reached ∼7. After being dried at 60 °C in a conventional oven for 2 days, the as-prepared sample was calcined in a muffle oven at 300 °C for 2 h under an argon atmosphere.

TiO$_2$-B nanoparticles/multiple-walled nanotubes (NP/MWNT) were synthesized in a similar manner, by only changing the amount of NaOH solution to 80 mL. TiO$_2$-B double-walled nanotubes (DWNT) were synthesized in a similar manner, by only changing the hydrothermal temperature to 150 °C. TiO$_2$-B nanoparticles/double-walled nanotubes (NP/DWNT) were synthesized in a similar manner, by changing both the amount of NaOH solution to 80 mL and the hydrothermal temperature to 150 °C.

Powder X-ray diffraction (XRD) was performed on a Rigaku D/max-2500 diffractometer operated in transmission mode with Cu Kα radiation. Transmission electron microscopy (TEM) was performed on either an FEI Tecnai 20 microscope or a Philips CM200 microscope. Brunauer−Emmett−Teller (BET) measurements to
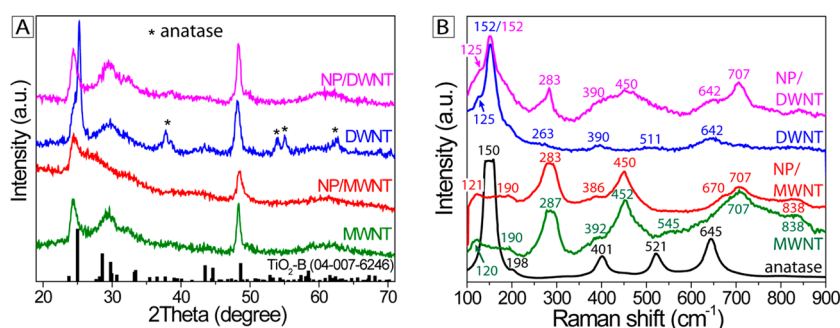
22200

dx.doi.org/10.1021/am505893q | ACS Appl. Mater. Interfaces 2014, 6, 22199−22208

Figure 2. (A) XRD data of four types of TiO_2-B based materials: MWNT (green), NP/MWNT (red), DWNT (blue), and NP/DWNT (pink). The black stick patterns present the TiO_2-B standard (JCPDS 46-1237); the asterisked peaks refer to anatase. (B) Raman spectra of four types of TiO_2-B based materials: MWNT (green), NP/MWNT (red), DWNT (blue), and NP/DWNT (pink). In addition, the spectrum of the precursor anatase (black) is also shown for comparison.

measure the specific surface areas of the obtained samples were carried out using a NOVA 2000e (Quantachrome) instrument, using nitrogen as the working gas. Raman spectroscopy was conducted on a laser confocal micro-Raman spectrometer (Horiba Jobin Yvon, LabRAM HR800), for which the laser wavelength was 532 nm, the laser power was 50 mW, the exposure time was 1 s, the number of scans was 50, and the spectral range was 100−900 cm^{-1}.

2.2. Electrochemical Analyses of Electrode Performance. Electrodes were prepared in an argon-filled glovebox (H_2O < 0.5 ppm and O_2 < 1 ppm) by mixing 75% of active material, 18% of acetylene black, and 7% of polyvinylidene fluoride (PVDF), and pressing the mixture into pellets.[19,24,46] All electrochemical analyses were conducted by using two-electrode Swagelok cells, in which a piece of lithium metal was used as the counter and reference electrode. The electrolyte was $LiPF_6$ (1 M) in a mixture of ethylene carbonate (EC) and diethyl carbonate (DEC) at a weight ratio of 1:1. The assembled cells were then taken out of the glovebox and sealed immediately with wax to prevent electrolyte leakage and/or air penetration during the subsequent electrochemical analyses. To study the charge capacity, cyclability, and rate capability, the standard galvanostatic technique was employed to discharge and charge the electrode at various current densities of 50−2000 mA/g, using a battery analyzer (MTI-BST8-MA, 10 mA). The cutoff potentials for charge and discharge were set at 3.0 and 1.0 V vs E_{Li/Li^+}, respectively. The cyclic voltammetry (CV) experiments were conducted on a potentiostat (Gamry Reference 600) at various scan rates of 0.1−1.0 mV/s. The electrochemical impedance spectroscopy (EIS) experiments were performed on a potentiostat (Zahner CIMPS-2) by using an alternating perturbation voltage of 5 mV in the frequency range of 0.01 Hz to 200 kHz.

3. RESULTS AND DISCUSSION

As shown by TEM images in Figure 1, a one-step hydrothermal method has been developed to synthesize hierarchical structures consisting of NPs-deposited NTs. The key experimental conditions are the reaction temperature and the amount of NaOH, that is, 140 °C/40 mL of NaOH solution for MWNT (Figure 1A), 140 °C/80 mL of NaOH solution for NP/MWNT (Figure 1B), 150 °C/40 mL of NaOH solution for DWNT (Figure 1C), and 150 °C/80 mL of NaOH solution for NP/DWNT (Figure 1D). In Figure 1A, the nanotubes are typically four layers, with the length of several hundred nanometers, outer diameters of approximately 10−15 nm, and an inner diameter of approximately 6−10 nm. When the NaOH amount is doubled (Figure 1B), instead of the original 1D structures,[47,54−57] 3D hierarchical structures of NPs (∼3 nm) deposited NTs are formed. When increasing the hydrothermal temperature to 150 °C, DWNTs are obtained (Figure 1C), with outer diameters of roughly 8−10 nm and inner diameters of roughly 5 nm. The inset in Figure 1C highlights an individual

DWNT. When both the hydrothermal temperature and the NaOH amount are changed, 3D hierarchical structures of NP/DWNT are produced (Figure 1D), where NPs are ∼3 nm in diameter. As shown by the top inset in Figure 1D, the continuous lattice fringes at the NP/NT interfaces indicate that the NP moieties are fused with NTs. Referring to the literature reports, which have only produced MWNTs,[47,54−57] the success of hierarchical structures herein is ascribed to the higher concentration of NaOH and longer reaction times. A widely accepted formation mechanism of TiO_2-B nanotubes is to scroll titanate (for example, $Na_2Ti_3O_7$) nanosheets,[48−52,54,58] which are *in situ* produced through the reaction between TiO_2 powder and NaOH. After the product is washed with HCl to perform the Na^+/H^+ ion exchange, $H_2Ti_3O_7 \cdot nH_2O$ nanotubes are produced,[52] during which the preformed $Na_2Ti_3O_7$ nanotubes act as templates. Next, calcination at elevated temperatures converts $H_2Ti_3O_7 \cdot nH_2O$ to TiO_2-B nanotubes.[52] Thus, the critical step is the formation of $Na_2Ti_3O_7$ nanotubes, for which the reaction temperature and the concentration of base are believed to control the reaction equilibrium, including the $Na_2Ti_3O_7$ monomer concentration, the dimensions of the $Na_2Ti_3O_7$ nanosheets, and the number of $Na_2Ti_3O_7$ stacking layers. If the hydrothermal temperature is above 150 °C, nanorods instead of NTs will be produced.[19,25,51,59] In addition, single-walled NTs remain a challenge to synthesize.[51]

Figure 2A shows the XRD data of the synthesized TiO_2-B MWNT (green), NP/MWNT (red), DWNT (blue), and NP/DWNT (pink). Except for DWNT, which contains a small amount of a-TiO_2, the crystalline phases in the other three samples seem to be phase-pure TiO_2-B.[15,36] The broadened diffraction peaks are typical features of nanomaterials.[24,60,61] However, it is well-known that XRD cannot detect very small crystals or amorphous compounds, which can be probed by Raman instead.[62] Thus, we performed Raman spectroscopy on these materials, as shown in Figure 2B. The precursor anatase shows all characteristic peaks as reported in the literature.[62] However, the spectra of the four materials are complicated, although the essential contribution can be confidently assigned to TiO_2-B. The computational results show that TiO_2-B has 18 Raman-active modes appearing at all positions of anatase's 8 Raman-active modes except for the one at 520 cm^{-1}.[63] The experimental results show that the Raman peak positions and relative intensities are dependent on the morphologies of the TiO_2-B nanostructures.[22,24,62,64,65] For instance, microflowers and nanosheets present the strongest peak at ∼256 cm^{-1} and do not have the peak at ∼150 cm^{-1}, whereas NPs present the
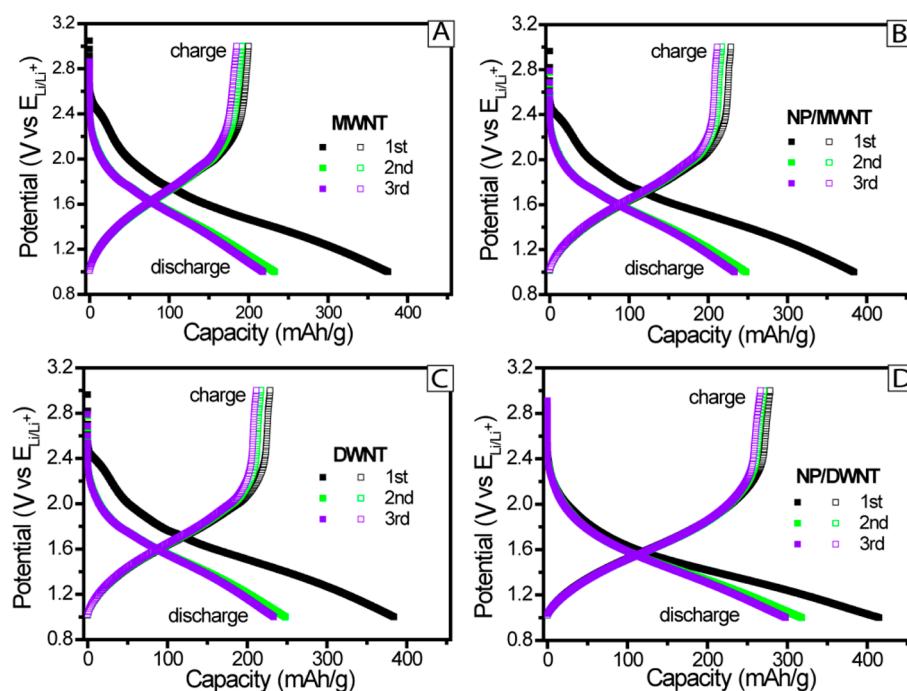
Figure 3. Potential−capacity plots for both discharge (lithiation) and charge (delithiation) processes during the first three cycles between 3.0 and 1.0 V at a current density of 50 mA/g for TiO_2-B electrodes made of MWNT (A), NP/MWNT (B), DWNT (C), and NP/DWNT (D).

strongest peak at 150 cm^{-1}.[22,64,65] Herein, MWNT and NP/MWNT have nearly identical profiles and neither of them show the peak at 150 cm^{-1}, which may be ascribed to the nature of MWNT, as microflowers and nanosheets.[22,64] A very weak band at 545 cm^{-1} in the case of MWNT could be assigned to the anatase impurity, corroborating the XRD result. In contrast, both DWNT and NP/DWNT show the strongest peak at 152 cm^{-1}; however, the assignment is difficult because anatase also has the strongest peak at the same position.[62] All other low intensity peaks can be assigned to TiO_2-B, except for the peak at 511 cm^{-1} in DWNT, which should be indexed to anatase.[62] In summary, the Raman results qualitatively support the XRD results and further suggest the possible existence of a small amount of anatase impurity in the MWNT sample. The further confirmation of the anatase impurities could be performed by analyzing the electrochemical results, as demonstrated in the literature and will be discussed below. It is noteworthy that Raman spectra of nanomaterials are often strongly dependent on the materials' morphologies, crystalline sizes, and wavelength of the excitation laser, for which carbon nanotubes and graphene nanosheets are good examples.[66−68] While the reasons for the a-TiO_2 impurity phase are unclear and will be studied in the future, we speculate that the hydrothermal temperature and the basicity of the reaction system play crucial roles.

The next structural characterization is the BET measurements, which reveal that the specific surface areas for MWNT, NP/MWNT, DWNT, and NP/DWNT are 155, 183, 212, and 246 m^2/g, respectively. These values indicate that the surface area of 3D hierarchical structures is 16% higher than that of 1D NTs and the surface area of DWNT samples is 35% higher than that of MWNTs.

After the basic characterization discussed above, the electrode performance of the four materials is then assessed using a series of electrochemical techniques. Figure 3 shows the potential−capacity profiles for both discharge (lithiation) and

charge (delithiation) processes during the first three cycles between 3.0 and 1.0 V at a current density of 50 mA/g. The sloping feature without voltage plateaus during the lithiation/delithiation cycles for all four samples suggests that the insertion/extraction of Li ions in the electrode occurs homogeneously without a phase transition between Li_xTiO_2 and TiO_2, behaving as in a solid solution that allows for a continuous change of x without causing any significant distortion of the structure.[9,22,69] Such a phenomenon has also been observed during the lithiation/delithiation processes of Nb_2O_5,[70] an anode material that, like TiO_2-B, presents a high rate capability due to the fast Li-ion transport in the infinite channels. The nature of this phenomenon is the pseudocapacitive discharging/charging process inside the bulk of the material, thus typically called intercalation pseudocapacitance.[70] While the electrode polarization that could, in principle, also induce a sloping profile cannot be ruled out, it is unlikely to play a significant role herein, as the electrode fabrication has used enough conductive additive (18% of acetylene black).[70] Moreover, a continuous lithiation/delithiation process free of phase-transition has been directly observed by Shahbazian-Yassar et al. in the case of studying amorphous TiO_2 nanowires with TEM.[71] The initial discharge capacities of these four samples are 375 mAh/g for MWNT, 384 mAh/g for the NP/MWNT, 398 mAh/g for DWNT, and 415 mAh/g for NP/DWNT, respectively. In the subsequent charge process, all of them exhibit some degree of irreversibility; that is, not all the inserted Li ions can be extracted. The irreversible capacities in the first cycle are 175 mAh/g for MWNT, 156 mAh/g for NP/MWNT, 153 mAh/g for DWNT, and 136 mAh/g for NP/DWNT, respectively. Evidently, DWNT materials present smaller irreversibility than MWNT materials; so do the 3D hierarchical NP/NT materials versus the 1D NT materials. The large capacity loss in the first cycle, a common phenomenon in most lithium intercalation hosts, is due to the irreversible reaction between TiO_2-B and the electrolyte to form the

lithium-containing solid electrolyte interphase (SEI).[5,7,60,72−75] In addition, some Li ions may also be trapped at grain boundaries or interstitial sites and then loose reversibility.[76−78] These results imply that, as expected, the superiority of NP/DWNT to others lies in the increased electrode/electrolyte contact area, the decreased reaction dimension for electrons and Li ions, and the enhanced capability for accommodating volume fluctuation.[7,14,30,3,34,54,79]

As discussed above (Figure 2), XRD and Raman detect the existence of anatase impurities in MWNT and DWNT. In the literature, the plot of differential capacity dQ/dV vs V has been demonstrated to be an effective approach to manifest trace amounts of anatase in TiO_2-B electrodes and reveal if the anatase phase contributes significantly to the charge capacity.[9,64] The principle is that a phase transition due to even a small amount of charge transfer will be embodied as a pair of sharp peaks (anodic and cathodic) in the dQ/dV vs V plot.[9,64] As shown in Figure 4, a pair of peaks at 1.96 V
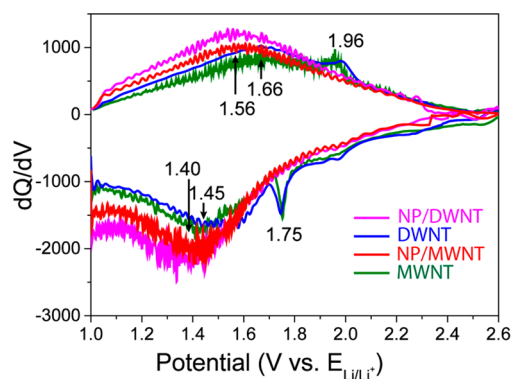

Figure 4. Plots of dQ/dV vs V extracted from the first cycle of potential−capacity plots in Figure 3.

(anodic) and 1.75 V (cathodic) resulting from anatase are indeed observed for both MWNT and DWNT electrodes.[13,62] Nevertheless, their weak intensities indicate that the anatase impurity has very limited contribution to the charge.[9,64] Besides these facts, all four materials show comparable profiles, which are characteristic with a pair of broad peaks centered at [1.56, 1.66] V and [1.40, 1.45] V, respectively. The broad features further corroborate the previous conclusion that the lithiation/delithiation process is essentially free of phase transition.[13,62,64]
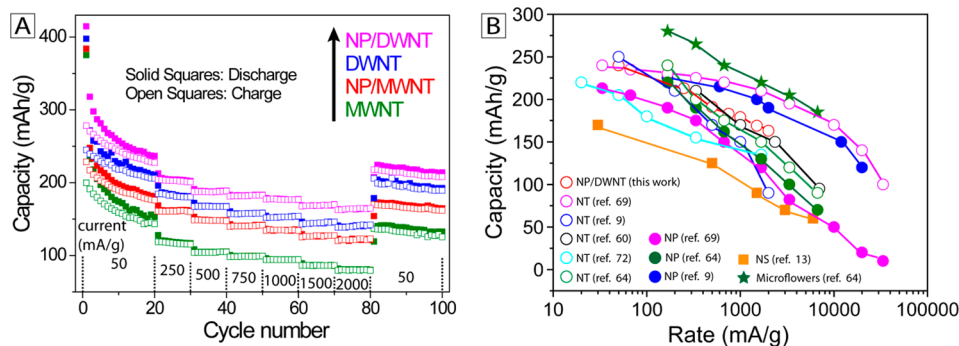
Next, the results of cyclability and rate capability are shown in Figure 5A. All battery cells are first cycled at 50 mA/g for 20 cycles, then at 250, 500, 750, 1000, 1500, and 2000 mA/g for 10 cycles each, and finally at 50 mA/g for 20 cycles. The capacities at various rates are summarized in Table S1 (Supporting Information). Similar to many other electrode materials, the capacities of the four materials herein decrease with increasing current densities.[64] Nevertheless, after 20 cycles, the capacity degradation is less than 0.1% per cycle. At the rate of 2000 mA/g, the capacity of NP/DWNT is still as high as 163 mAh/g. After changing the rate back to 50 mA/g, the capacities for all samples almost fully recovered, with 133 mAh/g for MWNT, 162 mAh/g for NP/MWNT, 192 mAh/g for DWNT, and 214 mAh/g for NP/DWNT. This excellent recoverability indicates the remarkable robustness of TiO_2-B NTs.[19,24,46,80] Figure 5B compares the performance of our NP/DWNT with the literature results of TiO_2-B nanostructures in different morphologies.[9,13,60,64,69,72] While our NP/DWNT (red open circle) is not the best, it ranks as the second among all NT-based materials and is inferior to only three systems, of which the hierarchical microflowers (denoted by green stars) is the best.[64]

To gain a deeper understanding of the performance-enhancement mechanism of NP/DWNT, we further compare the rate capability data with the BET data (Figure 6). As
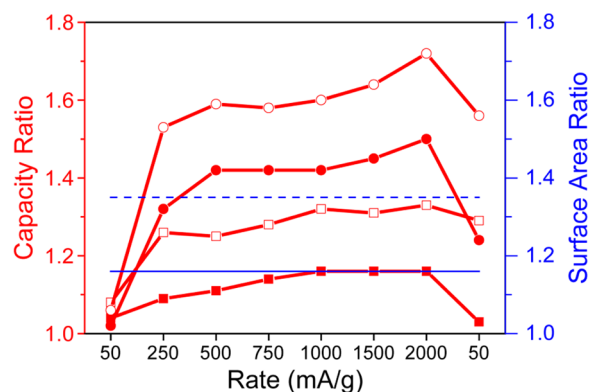

Figure 6. Comparison of capacity (Q) ratios with the corresponding surface area (S) ratios of the four TiO_2-B materials: (■) $Q_{NP/DWNT}:Q_{DWNT}$; (□) $Q_{NP/MWNT}:Q_{MWNT}$; (●) $Q_{NP/DWNT}:Q_{NP/MWNT}$; (○) $Q_{DWNT}:Q_{MWNT}$; (−) $S_{NP/DWNT}:S_{DWNT}$ and $S_{NP/MWNT}:S_{MWNT}$; and (---) $S_{NP/DWNT}:S_{NP/MWNT}$ and $S_{DWNT}:S_{MWNT}$.

Figure 5. (A) Rate capability of the four types of TiO_2-B electrodes at various charge/discharge rates of 50 mA/g for the first 20 cycles, then at 250, 500, 750, 1000, 1500, and 2000 mA/g for 10 cycles each, and finally at 50 mA/g for 20 cycles: MWNT (green), NP/MWNT (red), DWNT (blue), and NP/DWNT (pink). (B) Comparison of the rate capability between our NP/DWNT and the literature results of TiO_2-B nanostructures in different morphologies,[9,13,60,64,69,72] where NP denotes nanoparticles, DWNT denotes double-walled nanotubes, NT denotes nanotubes, and NS denotes nanosheets.
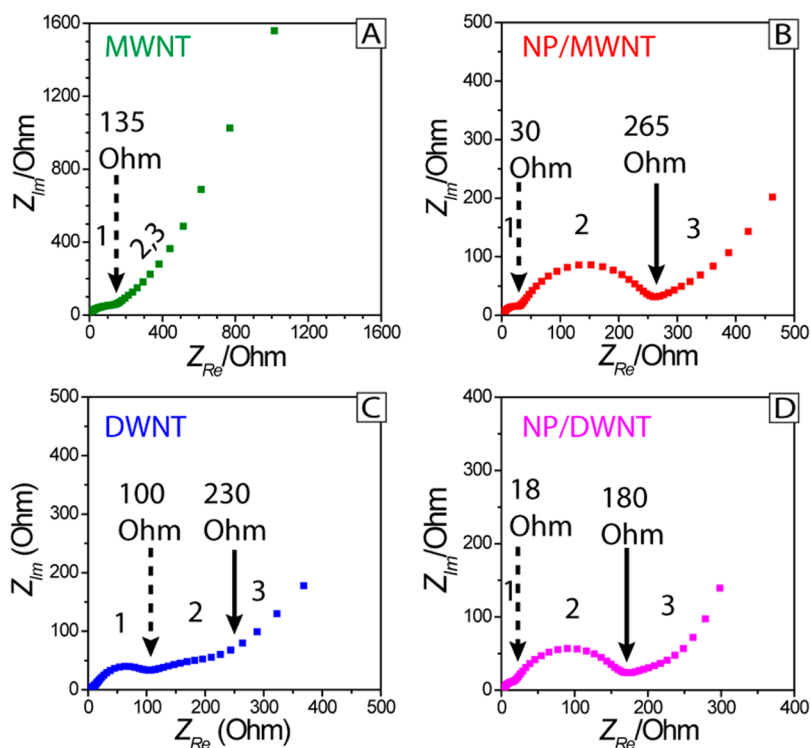
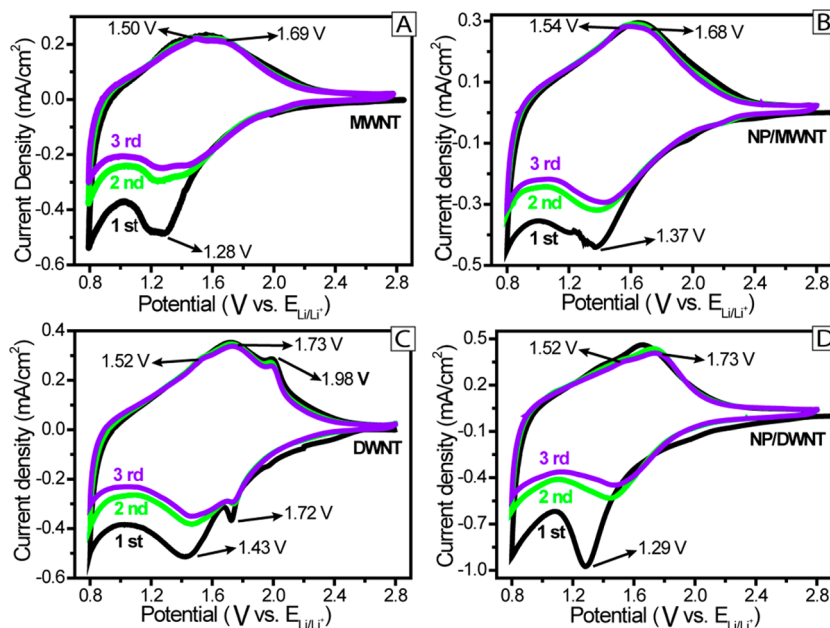**Figure 7.** EIS spectra of the four TiO_2-B materials taken at 1.0 V after the first discharge (lithiation).

Figure 8. Cyclic voltammograms of the four TiO_2-B materials for the first three cycles at a scan rate of 0.1 mV/s: MWNT (A), NP/MWNT (B), DWNT (C), and NP/DWNT (D).

mentioned above, the BET measurements reveal that specific surface areas (S) for MWNT, NP/MWNT, DWNT and NP/DWNT are 155, 183, 212, and 246 m^2/g, respectively. The corresponding ratios of $S_{NP/DWNT}:S_{DWNT}$ and $S_{NP/MWNT}:S_{MWNT}$ are both ~1.16, indicating a larger specific surface area of NP vs NT. In contrast, both ratios of $S_{NP/DWNT}:S_{NP/MWNT}$ and $S_{DWNT}:S_{MWNT}$ are 1.35, indicating a larger specific surface area of DWNT vs MWNT. In the first lithiation process at a small charge/discharge rate of 50 mA/g, all four ratios of $Q_{NP/DWNT}:Q_{DWNT}$ (■), $Q_{NP/MWNT}:Q_{MWNT}$ (□),

$Q_{NP/DWNT}:Q_{NP/MWNT}$ (●), and $Q_{DWNT}:Q_{MWNT}$ (○) are about 1. This result implies that all of these materials start with the same capability of hosting Li ions, which is essentially governed by the intrinsic properties of TiO_2-B,[9,60] regardless of the material morphologies (NP vs NT and DWNT vs MWNT) and the specific surface areas. With increasing the rate in the subsequent cycles, all four values increase dramatically. However, only $Q_{NP/DWNT}:Q_{DWNT}$ reaches its corresponding $S_{NP/DWNT}:S_{DWNT}$ (1.16, the solid blue line in Figure 6) at the rate of 1000 mA/g and keeps steady afterward; the other three
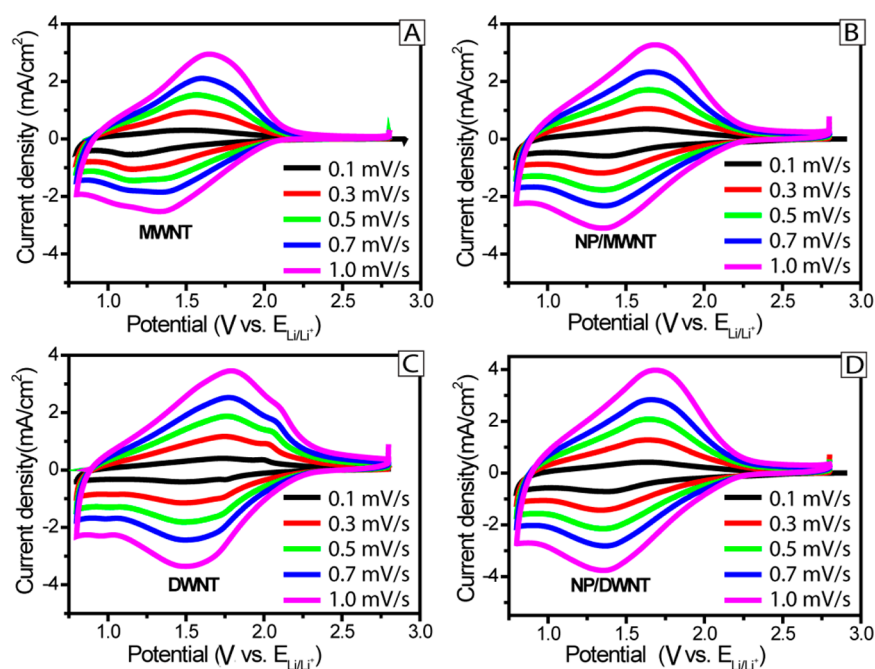
Figure 9. Cyclic voltammograms of four TiO_2-B materials at five various scan rates: MWNT (A), NP/MWNT (B), DWNT (C), and NP/DWNT (D).

ratios of $Q_{NP/MWNT}:Q_{MWNT}$, $Q_{NP/DWNT}:Q_{NP/MWNT}$, and $Q_{DWNT}:Q_{MWNT}$ are always above their corresponding $S_{NP/MWNT}:S_{MWNT}$ (1.16), $S_{NP/DWNT}:S_{NP/MWNT}$ (1.35), and $S_{DWNT}:S_{MWNT}$ (1.35), respectively. Moreover, after changing the rate back to 50 mA/g, only $Q_{NP/DWNT}:Q_{DWNT}$ returns to its initial value (1.03). These phenomena imply that the rate capability may be strongly correlated with the surface area.

On the other hand, it has also been reported that the Li-ion residing sites in TiO_2-B nanostructures are strongly dependent on their crystallographic orientations and morphologies.[20,22,64] Bartlett et al. reported that Li ions have the fastest travel speed along the $[1\bar{1}0]$ direction. The DFT+U (where DFT refers to density functional theory and U denotes internal potential) calculations by Stevenson et al. concluded that, for TiO_2-B nanoparticles, A2 sites near equatorial TiO_6 octahedra are filled first and A1 sites near axial TiO_6 octahedra are filled afterward.[22] In contrast, for TiO_2-B nanosheets, C sites are incrementally filled first, followed by A2 and A1 sites. Van der Ven et al. employed first-principles DFT calculations to study the thermodynamics of lithium-ion TiO_2-B and found that the preferred sites occupied by Li are A1 for $x \leq 0.5$, A2 and C for $x = 0.75$, and all sites (with increasing A1 occupation) at higher concentrations.[20] These studies demonstrate that the rate capability of TiO_2-B nanostructures would be strongly correlated with the Li-transport kinetics, on which electrochemical impedance spectroscopy (EIS) can shed light.[81] Figure 7 shows the EIS spectra of these electrodes taken at 1.0 V after the first lithiation. Indeed, these EIS spectra are quite different from each other. Each spectrum can be divided into three regions, of which the first one (a semicircle) results from the SEI formation resistance (R_{SEI}), the second one (also a semicircle) corresponds to the charge transfer resistance (R_{ct}) of Faradaic reactions, and the third one (a linear line) stems from the Warburg impedance (Z_W) due to the Li-ion diffusion inside TiO_2-B.[82] However, the amplitudes of these components are very different among these four materials. Whereas MWNT (A) and DWNT (C) show large R_{SEI} (>100 ohm), NP/MWNT

(B) and NP/DWNT (D) present much smaller R_{SEI} (<40 ohm). The disappearance of the second semicircle in (A) indicates that the Li-ion transport in MWNT is extremely sluggish.[83] In contrast, the other three systems show much faster Li-ion diffusion kinetics, among which NP/DWNT is superior to NP/MWNT and DWNT in R_{ct}. These results indicate that the different reaction kinetics in these four materials could also affect their rate capability dramatically.

Next, cyclic voltammetry is employed to study the electrode reactions of all four materials. Figure 8 shows their cyclic voltammograms (CVs) at a slow scan rate of 0.1 mV/s in the potential window of $[0.8, 2.8]$ V vs E_{Li/Li^+}. All samples display a pair of redox peaks, resulting from the pseudocapacitive Faradaic reactions of lithium storage in TiO_2-B,[7,21,24] at 1.28 V/$[1.50, 1.69]$ V for MWNT, 1.37 V/$[1.54, 1.68]$ V for NP/MWNT, 1.43 V/$[1.52, 1.73]$ V for DWNT, and 1.29 V/$[1.52, 1.73]$ V for NP/DWNT. The anodic peak in each case actually consists of two shoulder peaks, which are consistent with the literature report and ascribed to the Li extraction processes associated with different sites.[21,22] In the case of DWNT, another pair of small peaks at 1.72/1.98 V is assigned to the contribution from the a-TiO_2 impurity (as discussed above).[13,21] In addition, consistent with the capacity data in Figure 3, there is a significant current-intensity loss in the second cycle compared with the first cycle for every sample; the difference between the third cycle and the second cycle is fairly small.

Furthermore, the extensive study of CVs at five different scan rates is showed in Figure 9. All four samples show similar behaviors: the intensities of both cathodic (discharge) and anodic (charge) currents increase with the scan rate over the entire potential window. The slight peak potential shifts ($\Delta E_{anodic} = [0.04-0.06]$ V and $\Delta E_{cathodic} = [0-0.03]$ V) in all cases indicate that there is not serious electrode polarization or phase transition, similar to Nb_2O_5 as reported.[70] Furthermore, to gain a deeper understanding of the nature of both anodic and cathodic currents, the peak current density (j_p) is plotted

against the scan rate (ν) in the format of log (j_p)−log (ν), by assuming that j_p follows a power-law relationship with ν (eq 1)[70]

$$j_p \propto \nu^z \qquad (1)$$

where the power z indicates the nature of the current: a value of 0.5 would indicate that the current is controlled by semi-infinite linear diffusion; a value of 1 would indicate that the current is surface-controlled.[70] In all cases (Figure 10), the z value for the
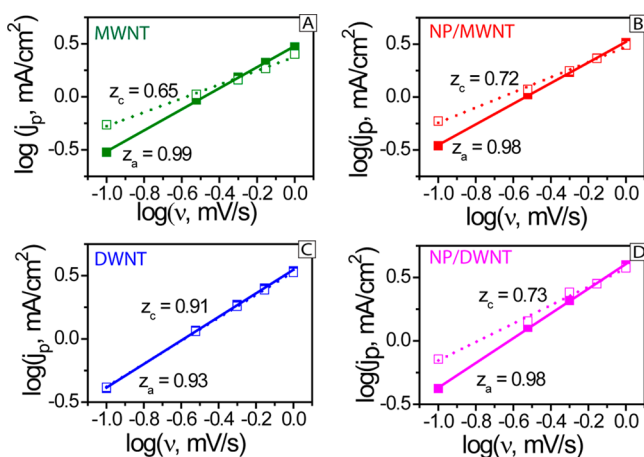

Figure 10. Plots of log (current density)−log (scan rate), that is, log (j_p, mA/cm^2)−log (ν, mV/s), based on the cyclic voltammograms in Figure 9, for MWNT (A), NP/MWNT (B), DWNT (C), and NP/DWNT (D). The values of z_a and z_c are from the fitting slopes of solid squares and open squares, respectively.

anodic peak (z_a, the slope of the fitting line for the solid squares) is about 1, indicating the nature of the pseudocapacitive current during the delithiation process.[84−86] Additionally, the z_c value (the slope of the fitting line for the open squares) for DWNT ($z_c = 0.91$) is also close to 1, implying the fast Li-ion transport even during the lithiation process in this material. In contrast, the other three materials show z_c values around 0.7, which means that the lithiation process is governed by both diffusion in the bulk and the reaction on the surface.[70]

4. CONCLUSION

In conclusion, we have reported a novel 3D hierarchical structure of TiO$_2$-B NP/DWNT, which presents enhanced electrode performance as the anode material in LIBs, compared with three other structures of MWNT, NP/MWNT, and DWNT. All four types of materials are synthesized through a one-step hydrothermal process from anatase powders and NaOH, followed by calcination at 300 °C for 2 h under argon. The key factors for obtaining NP/DWNT are the high alkaline concentration, the appropriate reaction duration (48 h), and the optimal reaction temperature (150 °C). On the basis of a series of studies, we can draw the following conclusions: (1) At high rates, the Li-ion transport kinetics and the surface area both play important roles in charge capacity; in other words, the high rate capability lies in the pseudocapacitive nature of the lithiation/delithiation processes both in the bulk and on the surface. (2) NP and DWNT present comparable performance in specific charge capacity and cycling stability, but different reaction kinetics. (3) The inner space of DWNT and MWNT, as their outer space, may also be readily accessible for Li ions. (4) The superiority of DWNT to MWNT lies in the fewer

layers of tubes, rendering a shorter transport distance for Li ions through the radial direction, the predominate (or even probably the only) lithiation direction. Thus, the performance enhancement can be assigned to not only NPs (only ∼3 nm in diameter), which increase surface areas and decrease diffusion lengths of electrons and Li ions, but also the thinner walls of DWNTs, which allows for efficient lithium transport through the radial direction inside and outside of NTs. The capacity of NP/DWNT can reach as high as 163 mAh/g even at the rate of 2000 mA/g; this performance is among the best regarding all TiO$_2$-B nanostructures. In addition, the synthetic strategy of producing hierarchical NP/DWNT structures in one step, which is demonstrated in this work, may also be applicable to other battery materials.

■ ASSOCIATED CONTENT

ⓢ Supporting Information

A table showing the specific capacity of all four materials at various charge/discharge rates and their capacity ratios. This material is available free of charge via the Internet at http://pubs.acs.org.

■ AUTHOR INFORMATION

Corresponding Authors
*E-mail: dingjn@cczu.edu.cn (J.D.).
*E-mail: yonyang@mines.edu (Y.Y.).

Author Contributions

The manuscript was written through contributions of all authors. All authors have given approval to the final version of the manuscript.

Notes

The authors declare no competing financial interest.

■ REFERENCES

(1) Tarascon, J. M.; Armand, M. Issues and Challenges Facing Rechargeable Lithium Batteries. *Nature* **2001**, *414*, 359−367.
(2) Whittingham, M. S. History, Evolution, and Future Status of Energy Storage. *Proc. IEEE* **2012**, *100*, 1518−1534.
(3) Zhu, H. Y.; Lan, Y.; Gao, X. P.; Ringer, S. P.; Zheng, Z. F.; Song, D. Y.; Zhao, J. C. Phase Transition between Nanostructures of Titanate and Titanium Dioxides via Simple Wet-Chemical Reactions. *J. Am. Chem. Soc.* **2005**, *127*, 6730−6736.
(4) Marom, R.; Amalraj, S. F.; Leifer, N.; Jacob, D.; Aurbach, D. A Review of Advanced and Practical Lithium Battery Materials. *J. Mater. Chem.* **2011**, *21*, 9938−9954.
(5) Cheng, F. Y.; Liang, J.; Tao, Z. L.; Chen, J. Functional Materials for Rechargeable Batteries. *Adv. Mater.* **2011**, *23*, 1695−1715.
(6) Ren, Y.; Hardwick, L. J.; Bruce, P. G. Lithium Intercalation into Mesoporous Anatase with an Ordered 3D Pore Structure. *Angew. Chem., Int. Ed.* **2010**, *49*, 2570−2574.
(7) Liu, H. S.; Bi, Z. H.; Sun, X. G.; Unocic, R. R.; Paranthaman, M. P.; Dai, S.; Brown, G. M. Mesoporous TiO$_2$-B Microspheres with

Superior Rate Performance for Lithium Ion Batteries. *Adv. Mater.* **2011**, *23*, 3450−3454.

(8) Wu, H. B.; Chen, J. S.; Hng, H. H.; Lou, X. W. Nanostructured Metal Oxide-Based Materials as Advanced Anodes for Lithium-Ion Batteries. *Nanoscale* **2012**, *4*, 2526−2542.

(9) Ren, Y.; Liu, Z.; Pourpoint, F.; Armstrong, A. R.; Grey, C. P.; Bruce, P. G. Nanoparticulate TiO$_2$(B): An Anode for Lithium-Ion Batteries. *Angew. Chem., Int. Ed.* **2012**, *51*, 2164−2167.

(10) Zhen, M.; Su, L.; Yuan, Z.; Liu, L.; Zhou, Z. Well-Distributed TiO$_2$ Nanocrystals on Reduced Graphene Oxides as High-Performance Anode Materials for Lithium Ion Batteries. *RSC Adv.* **2013**, *3*, 13696−13701.

(11) Zhen, M.; Guo, X.; Gao, G.; Zhou, Z.; Liu, L. Rutile TiO$_2$ Nanobundles on Reduced Graphene Oxides as Anode Materials for Li Ion Batteries. *Chem. Commun.* **2014**, *50*, 11915−11918.

(12) Qu, J.; Wu, Q. D.; Ren, Y. R.; Su, Z.; Lai, C.; Ding, J. N. Enhanced High-Rate Performance of Double-Walled TiO$_2$-B Nanotubes as Anodes in Lithium-Ion Batteries. *Chem.—Asian J.* **2012**, *7*, 2516−2518.

(13) Chen, C. J.; Hu, X. L.; Wang, Z. H.; Xiong, X. Q.; Hu, P.; Liu, Y.; Huang, Y. H. Controllable Growth of TiO$_2$-B Nanosheet Arrays on Carbon Nanotubes as a High-Rate Anode Material for Lithium-Ion Batteries. *Carbon* **2014**, *69*, 302−310.

(14) Giannuzzi, R.; Manca, M.; De Marco, L.; Belviso, M. R.; Cannavale, A.; Sibillano, T.; Giannini, C.; Cozzoli, P. D.; Gigli, G. Ultrathin TiO$_2$(B) Nanorods with Superior Lithium-Ion Storage Performance. *ACS Appl. Mater. Interfaces* **2014**, *6*, 1933−1943.

(15) Marchand, R.; Brohan, L.; Tournoux, M. TiO$_2$(B) a New Form of Titanium-Dioxide and the Potassium Octatitanate K$_2$Ti$_8$O$_{17}$. *MRS Bull.* **1980**, *15*, 1129−1133.

(16) Tournoux, M.; Marchand, R.; Brohan, L. Layered K$_2$Ti$_4$O$_9$ and the Open Metastable TiO$_2$(B) Structure. *Prog. Solid State Chem.* **1986**, *17*, 33−52.

(17) Kasuga, T.; Hiramatsu, M.; Hoson, A.; Sekino, T.; Niihara, K. Formation of Titanium Oxide Nanotube. *Langmuir* **1998**, *14*, 3160−3163.

(18) Feist, T. P.; Davies, P. K. The Soft Chemical Synthesis of TiO$_2$ (B) from Layered Titanates. *J. Solid State Chem.* **1992**, *101*, 275−295.

(19) Armstrong, A. R.; Armstrong, G.; Canales, J.; Garcia, R.; Bruce, P. G. Lithium-Ion Intercalation into TiO$_2$-B Nanowires. *Adv. Mater.* **2005**, *17*, 862−865.

(20) Dalton, A. S.; Belak, A. A.; Van der Ven, A. Thermodynamics of Lithium in TiO$_2$(B) from First Principles. *Chem. Mater.* **2012**, *24*, 1568−1574.

(21) Zukalova, M.; Kalbac, M.; Kavan, L.; Exnar, I.; Graetzel, M. Pseudocapacitive Lithium Storage in TiO$_2$(B). *Chem. Mater.* **2005**, *17*, 1248−1255.

(22) Dylla, A. G.; Xiao, P. H.; Henkelman, G.; Stevenson, K. J. Morphological Dependence of Lithium Insertion in Nanocrystalline TiO$_2$(B) Nanoparticles and Nanosheets. *J. Phys. Chem. Lett.* **2012**, *3*, 2015−2019.

(23) Dylla, A. G.; Henkelman, G.; Stevenson, K. J. Lithium Insertion in Nanostructured TiO$_2$(B) Architectures. *Acc. Chem. Res.* **2013**, *46*, 1104−1112.

(24) Armstrong, A. R.; Armstrong, G.; Canales, J.; Bruce, P. G. TiO$_2$-B Nanowires. *Angew. Chem., Int. Ed.* **2004**, *43*, 2286−2288.

(25) Wang, G.; Wang, Q.; Lu, W.; Li, J. H. Photoelectrochemical Study on Charge Transfer Properties of TiO$_2$-B Nanowires with an Application as Humidity Sensors. *J. Phys. Chem. B* **2006**, *110*, 22029−22034.

(26) Yang, Z. G.; Choi, D.; Kerisit, S.; Rosso, K. M.; Wang, D. H.; Zhang, J.; Graff, G.; Liu, J. Nanostructures and Lithium Electrochemical Reactivity of Lithium Titanites and Titanium Oxides: A Review. *J. Power Sources* **2009**, *192*, 588−598.

(27) Bruce, P. G.; Scrosati, B.; Tarascon, J. M. Nanomaterials for Rechargeable Lithium Batteries. *Angew. Chem., Int. Ed.* **2008**, *47*, 2930−2946.

(28) Rai, A. K.; Anh, L. T.; Gim, J.; Mathew, V.; Kang, J.; Paul, B. J.; Song, J.; Kim, J. Simple Synthesis and Particle Size Effects of TiO$_2$ Nanoparticle Anodes for Rechargeable Lithium Ion Batteries. *Electrochim. Acta* **2013**, *90*, 112−118.

(29) Kang, J. W.; Kim, D. H.; Mathew, V.; Lim, J. S.; Gim, J. H.; Kimz, J. Particle Size Effect of Anatase TiO$_2$ Nanocrystals for Lithium-Ion Batteries. *J. Electrochem. Soc.* **2011**, *158*, A59−A62.

(30) Wang, J.; Polleux, J.; Lim, J.; Dunn, B. Pseudocapacitive Contributions to Electrochemical Energy Storage in TiO$_2$ (Anatase) Nanoparticles. *J. Phys. Chem. C* **2007**, *111*, 14925−14931.

(31) Kim, C.; Noh, M.; Choi, M.; Cho, J.; Park, B. Critical Size of a Nano SnO$_2$ Electrode for Li-Secondary Battery. *Chem. Mater.* **2005**, *17*, 3297−3301.

(32) Oh, S. W.; Park, S. H.; Sun, Y. K. Hydrothermal Synthesis of Nano-Sized Anatase TiO$_2$ Powders for Lithium Secondary Anode Materials. *J. Power Sources* **2006**, *161*, 1314−1318.

(33) Sudant, G.; Baudrin, E.; Larcher, D.; Tarascon, J. M. Electrochemical Lithium Reactivity with Nanotextured Anatase-Type TiO$_2$. *J. Mater. Chem.* **2005**, *15*, 1263−1269.

(34) Wagemaker, M.; Borghols, W. J. H.; Mulder, F. M. Large Impact of Particle Size on Insertion Reactions. A Case for Anatase Li$_x$TiO$_2$. *J. Am. Chem. Soc.* **2007**, *129*, 4323−4327.

(35) Nian, J. N.; Teng, H. S. Hydrothermal Synthesis of Single-Crystalline Anatase TiO$_2$ Nanorods with Nanotubes as the Precursor. *J. Phys. Chem. B* **2006**, *110*, 4193−4198.

(36) Li, J. M.; Wan, W.; Zhou, H. H.; Li, J. J.; Xu, D. S. Hydrothermal Synthesis of TiO$_2$(B) Nanowires with Ultrahigh Surface Area and Their Fast Charging and Discharging Properties in Li-Ion Batteries. *Chem. Commun.* **2011**, *47*, 3439−3441.

(37) Wang, B.; Cheng, J. L.; Wu, Y. P. Titania Nanotube Synthesized by a Facile, Scalable and Cheap Hydrolysis Method for Reversible Lithium-Ion Batteries. *J. Alloys Compd.* **2012**, *527*, 132−136.

(38) Wang, H. E.; Chen, Z. H.; Leung, Y. H.; Luan, C. Y.; Liu, C. P.; Tang, Y. B.; Yan, C.; Zhang, W. J.; Zapien, J. A.; Bello, I.; Lee, S. T. Hydrothermal Synthesis of Ordered Single-Crystalline Rutile TiO$_2$ Nanorod Arrays on Different Substrates. *Appl. Phys. Lett.* **2010**, *96*, No. 263104.

(39) An, L. P.; Gao, X. P.; Li, G. R.; Yan, T. Y.; Zhu, H. Y.; Shen, P. W. Electrochemical Lithium Storage of Titania Nanotubes Modified with NiO Nanoparticles. *Electrochim. Acta* **2008**, *53*, 4573−4579.

(40) Hu, L. B.; Wu, H.; Hong, S. S.; Cui, L. F.; McDonough, J. R.; Bohy, S.; Cui, Y. Si Nanoparticle-Decorated Si Nanowire Networks for Li-Ion Battery Anodes. *Chem. Commun.* **2011**, *47*, 367−369.

(41) Wang, L. L.; Zhang, S. C.; Wu, X. M. Synthesis and Lithium Storage Properties of NiO@TiO$_2$ Nanotube Heterojunction Arrays. *Chem. Lett.* **2011**, *40*, 1428−1430.

(42) Fan, Y. Q.; Zhang, N.; Zhang, L. Y.; Shao, H. B.; Wang, J. M.; Zhang, J. Q.; Cao, C. N. Co$_3$O$_4$-Coated TiO$_2$ Nanotube Composites Synthesized through Photo-Deposition Strategy with Enhanced Performance for Lithium-Ion Batteries. *Electrochim. Acta* **2013**, *94*, 285−293.

(43) Guan, D. S.; Li, J. Y.; Gao, X. F.; Yuan, C. Controllable Synthesis of MoO$_3$-Deposited TiO$_2$ Nanotubes with Enhanced Lithium-Ion Intercalation Performance. *J. Power Sources* **2014**, *246*, 305−312.

(44) Yu, L.; Wang, Z. Y.; Zhang, L.; Wu, H. B.; Lou, X. W. TiO$_2$ Nanotube Arrays Grafted with Fe$_2$O$_3$ Hollow Nanorods as Integrated Electrodes for Lithium-Ion Batteries. *J. Mater. Chem. A* **2013**, *1*, 122−127.

(45) Zhang, J. W.; Jin, Z. S.; Wu, Z. S.; Zhang, Z. J. Electrochemical Lithium Storage Capacity of Nickel Mono-Oxide Loaded Anatase Titanium Dioxide Nanotubes. *Ionics* **2012**, *18*, 861−866.

(46) Armstrong, G.; Armstrong, A. R.; Canales, J.; Bruce, P. G. Nanotubes with the TiO$_2$-B Structure. *Chem. Commun.* **2005**, 2454−2456.

(47) Bavykin, D. V.; Lapkin, A. A.; Plucinski, P. K.; Friedrich, J. M.; Walsh, F. C. Reversible Storage of Molecular Hydrogen by Sorption into Multilayered TiO$_2$ Nanotubes. *J. Phys. Chem. B* **2005**, *109*, 19422−19427.

(48) Wang, Y. Q.; Hu, G. Q.; Duan, X. F.; Sun, H. L.; Xue, Q. K. Microstructure and Formation Mechanism of Titanium Dioxide Nanotubes. *Chem. Phys. Lett.* **2002**, *365*, 427−431.

(49) Chen, Q.; Du, G. H.; Zhang, S.; Peng, L. M. The Structure of Trititanate Nanotubes. *Acta Crystallogr., Sect. B: Struct. Sci.* **2002**, *58*, 587−593.

(50) Chen, Y. F.; Lee, C. Y.; Yeng, M. Y.; Chiu, H. T. Preparing Titanium Oxide with Various Morphologies. *Mater. Chem. Phys.* **2003**, *81*, 39−44.

(51) Yoshida, R.; Suzuki, Y.; Yoshikawa, S. Syntheses of $TiO_2(B)$ Nanowires and TiO_2 Anatase Nanowires by Hydrothermal and Post-Heat Treatments. *J. Solid State Chem.* **2005**, *178*, 2179−2185.

(52) Suzuki, Y.; Yoshikawa, S. Synthesis and Thermal Analyses of TiO_2-Derived Nanotubes Prepared by the Hydrothermal Method. *J. Mater. Res.* **2004**, *19*, 982−985.

(53) Yoshida, R.; Suzuki, Y.; Yoshikawa, S. Effects of Synthetic Conditions and Heat-Treatment on the Structure of Partially Ion-Exchanged Titanate Nanotubes. *Mater. Chem. Phys.* **2005**, *91*, 409−416.

(54) Kuho, T.; Nakahira, A. Local Structure of TiO_2-Derived Nanotubes Prepared by the Hydrothermal Process. *J. Phys. Chem. C* **2008**, *112*, 1658−1662.

(55) Nakahira, A.; Kubo, T.; Yamasaki, Y. Microstructural Control of Mesoporous Bulk Composed of TiO_2-Derived Titanate Nanotubes. *ACS Appl. Mater. Interfaces* **2010**, *2*, 1136−1140.

(56) Miao, L.; Tanemura, S.; Huang, R.; Liu, C. Y.; Huang, C. M.; Xu, G. Large Seebeck Coefficients of Protonated Titanate Nanotubes for High-Temperature Thermoelectric Conversion. *ACS Appl. Mater. Interfaces* **2010**, *2*, 2355−2359.

(57) Cesano, F.; Bertarione, S.; Uddin, M. J.; Agostini, G.; Scarano, D.; Zecchina, A. Designing TiO_2 Based Nanostructures by Control of Surface Morphology of Pure and Silver Loaded Titanate Nanotubes. *J. Phys. Chem. C* **2010**, *114*, 169−178.

(58) Feist, T. P.; Mocarski, S. J.; Davies, P. K.; Jacobson, A. J.; Lewandowski, J. T. Formation of $TiO_2(B)$ by Proton Exchange and Thermolysis of Several Alkali Metal Titanate Structures. *Solid State Ionics* **1988**, *28−30* (Part 2), 1338−1343.

(59) Jitputti, J.; Suzuki, Y.; Yoshikawa, S. Synthesis of TiO_2 Nanowires and Their Photocatalytic Activity for Hydrogen Evolution. *Catal. Commun.* **2008**, *9*, 1265−1271.

(60) Armstrong, G.; Armstrong, A. R.; Canales, J.; Bruce, P. G. $TiO_2(B)$ Nanotubes as Negative Electrodes for Rechargeable Lithium Batteries. *Electrochem. Solid-State Lett.* **2006**, *9*, A139−A143.

(61) Li, Q. J.; Zhang, J. W.; Liu, B. B.; Li, M.; Liu, R.; Li, X. L.; Ma, H. L.; Yu, S. D.; Wang, L.; Zou, Y. G.; Li, Z. P.; Zou, B.; Cui, T.; Zou, G. T. Synthesis of High-Density Nanocavities Inside $TiO_2−B$ Nanoribbons and Their Enhanced Electrochemical Lithium Storage Properties. *Inorg. Chem.* **2008**, *47*, 9870−9873.

(62) Beuvier, T.; Richard-Plouet, M.; Brohan, L. Accurate Methods for Quantifying the Relative Ratio of Anatase and $TiO_2(B)$ Nanoparticles. *J. Phys. Chem. C* **2009**, *113*, 13703−13706.

(63) Ben Yahia, M.; Lemoigno, F.; Beuvier, T.; Filhol, J. S.; Richard-Plouet, M.; Brohan, L.; Doublet, M. L. Updated References for the Structural, Electronic, and Vibrational Properties of TiO2(B) Bulk using First-Principles Density Functional Theory Calculations. *J. Chem. Phys.* **2009**, *130*, No. 204501.

(64) Etacheri, V.; Kuo, Y. T.; Van der Ven, A.; Bartlett, B. M. Mesoporous $TiO_2−B$ Microflowers Composed of $(1\bar{1}0)$ Facet-Exposed Nanosheets for Fast Reversible Lithium-Ion Storage. *J. Mater. Chem. A* **2013**, *1*, 12028−12032.

(65) Kobayashi, M.; Petrykin, V. V.; Kakihana, M. One-Step Synthesis of $TiO_2(B)$ Nanoparticles from a Water-Soluble Titanium Complex. *Chem. Mater.* **2007**, *19*, 5373−5376.

(66) Soin, N.; Roy, S. S.; Ray, S. C.; McLaughlin, J. A. Excitation Energy Dependence of Raman Bands in Multiwalled Carbon Nanotubes. *J. Raman Spectrosc.* **2010**, *41*, 1227−1233.

(67) Ferrari, A. C. Raman Spectroscopy of Graphene and Graphite: Disorder, Electron-Phonon Coupling, Doping and Nonadiabatic Effects. *Solid State Commun.* **2007**, *143*, 47−57.

(68) Dresselhaus, M. S.; Jorio, A.; Hofmann, M.; Dresselhaus, G.; Saito, R. Perspectives on Carbon Nanotubes and Graphene Raman Spectroscopy. *Nano Lett.* **2010**, *10*, 751−758.

(69) Shin, K.; Kim, H. J.; Choi, J. M.; Choi, Y. M.; Song, M. S.; Park, J. H. Controlled Synthesis of Skein Shaped $TiO_2−B$ Nanotube Cluster Particles with Outstanding Rate Capability. *Chem. Commun.* **2013**, *49*, 2326−2328.

(70) Augustyn, V.; Come, J.; Lowe, M. A.; Kim, J. W.; Taberna, P. L.; Tolbert, S. H.; Abruna, H. D.; Simon, P.; Dunn, B. High-Rate Electrochemical Energy Storage through Li^+ Intercalation Pseudocapacitance. *Nat. Mater.* **2013**, *12*, 518−522.

(71) Gao, Q.; Gu, M.; Nie, A.; Mashayek, F.; Wang, C.; Odegard, G. M.; Shahbazian-Yassar, R. Direct Evidence of Lithium-Induced Atomic Ordering in Amorphous TiO_2 Nanotubes. *Chem. Mater.* **2014**, *26*, 1660−1669.

(72) Brutti, S.; Gentili, V.; Menard, H.; Scrosati, B.; Bruce, P. G. TiO_2-(B) Nanotubes as Anodes for Lithium Batteries: Origin and Mitigation of Irreversible Capacity. *Adv. Energy Mater.* **2012**, *2*, 322−327.

(73) Liu, S. H.; Jia, H. P.; Han, L.; Wang, J. L.; Gao, P. F.; Xu, D. D.; Yang, J.; Che, S. N. Nanosheet-Constructed Porous $TiO_2−B$ for Advanced Lithium Ion Batteries. *Adv. Mater.* **2012**, *24*, 3201−3204.

(74) Wang, Z. Y.; Zhou, L.; Lou, X. W. Metal Oxide Hollow Nanostructures for Lithium-Ion Batteries. *Adv. Mater.* **2012**, *24*, 1903−1911.

(75) Liu, S. H.; Wang, Z. Y.; Yu, C.; Wu, H. B.; Wang, G.; Dong, Q.; Qiu, J. S.; Eychmuller, A.; Lou, X. W. A Flexible $TiO_2(B)$-Based Battery Electrode with Superior Power Rate and Ultralong Cycle Life. *Adv. Mater.* **2013**, *25*, 3462−3467.

(76) Liu, D. W.; Xiao, P.; Zhang, Y. H.; Garcia, B. B.; Zhang, Q. F.; Guo, Q.; Champion, R.; Cao, G. Z. TiO_2 Nanotube Arrays Annealed in N_2 for Efficient Lithium-Ion Intercalation. *J. Phys. Chem. C* **2008**, *112*, 11175−11180.

(77) Wang, Q.; Wen, Z. H.; Li, J. H. Solvent-Controlled Synthesis and Electrochemical Lithium Storage of One-Dimensional TiO_2 Nanostructures. *Inorg. Chem.* **2006**, *45*, 6944−6949.

(78) Zhu, K.; Wang, Q.; Kim, J. H.; Pesaran, A. A.; Frank, A. J. Pseudocapacitive Lithium-Ion Storage in Oriented Anatase TiO_2 Nanotube Arrays. *J. Phys. Chem. C* **2012**, *116*, 11895−11899.

(79) Armstrong, A. R.; Arrouvel, C.; Gentili, V.; Parker, S. C.; Islam, M. S.; Bruce, P. G. Lithium Coordination Sites in $Li_xTiO_2(B)$: A Structural and Computational Study. *Chem. Mater.* **2010**, *22*, 6426−6432.

(80) Zhang, H.; Li, G. R.; An, L. P.; Yan, T. Y.; Gao, X. P.; Zhu, H. Y. Electrochemical Lithium Storage of Titanate and Titania Nanotubes and Nanorods. *J. Phys. Chem. C* **2007**, *111*, 6143−6148.

(81) Shin, J. Y.; Joo, J. H.; Samuelis, D.; Maier, J. Oxygen-Deficient $TiO_{2−δ}$ Nanoparticles via Hydrogen Reduction for High Rate Capability Lithium Batteries. *Chem. Mater.* **2012**, *24*, 543−551.

(82) Favors, Z.; Wang, W.; Bay, H. H.; Mutlu, Z.; Ahmed, K.; Liu, C.; Ozkan, M.; Ozkan, C. S. Scalable Synthesis of Nano-Silicon from Beach Sand for Long Cycle Life Li-ion Batteries. *Sci. Rep.* **2014**, *4*, No. 5623.

(83) Bard, A. J.; Faulkner, L. R. *Electrochemical Methods: Fundamentals and Applications*, 2nd ed.; John Wiley & Sons, Inc.: New York, 2001.

(84) Li, J. R.; Tang, Z. L.; Zhang, Z. T. Pseudocapacitive Characteristic of Lithium Ion Storage in Hydrogen Titanate Nanotubes. *Chem. Phys. Lett.* **2006**, *418*, 506−510.

(85) Nuspl, G.; Yoshizawa, K.; Yamabe, T. Lithium Intercalation in TiO_2 Modifications. *J. Mater. Chem.* **1997**, *7*, 2529−2536.

(86) Zukalova, M.; Kalbac, M.; Kavan, L.; Exnar, I.; Haeger, A.; Graetzel, M. Electrochemical and Gas-Phase Photocatalytic Performance of Nanostructured $TiO_2(B)$ Prepared by Novel Synthetic Route. *Prog. Solid State Chem.* **2005**, *33*, 253−261.